A Compact Dual-Band Implantable Antenna for Wireless Biotelemetry in Arteriovenous Grafts

Jungang Zhang, *Student Member, IEEE*, Rupam Das, *Senior Member, IEEE*,
Daniel Hoare, *Member, IEEE*, Huxi Wang, *Student Member, IEEE*, Afesomeh Ofiare,
Nosrat Mirzai, *Member, IEEE*, John Mercer, and Hadi Heidari, *Senior Member, IEEE*

Abstract— Arteriovenous grafts (AVGs) are indispensable life-saving implants for chronic kidney disease (CKD) patients undergoing hemodialysis (HD). However, AVGs will often fail due to postoperative complications, such as cellular accumulation termed restenosis, blood clots, and infections, which are dominant causes of morbidity and mortality. A new generation of HD implants equipped with biosensors and multiband antennas for wireless power and telemetry systems that can detect specific pathological parameters and report AVGs' patency would be transformative for CKD. Our study proposes a compact dual-band implantable antenna for HD monitoring applications. It operates in 1.4 and 2.45 GHz for wireless power transfer and biotelemetry purposes. The miniaturized antenna with a current size of 5 × 5 × 0.635 mm³ exhibits wide bandwidth (300 MHz at 1.4-GHz band and 380 MHz at 2.45-GHz band), along with good impedance matching at two resonance frequencies. In addition, simulations are performed separately in a three-layer homogenous phantom and a realistic human body model. Measurements of the proposed antenna are evaluated in minced pork. The measured results of the fabricated antenna prototype are closely harmonized with the simulation ones, and the effect of different proportions of fat tissue in pork mince was analyzed to verify the sensitivity of the antenna to the contacting medium. The specific absorption rate (SAR) and link budget calculation are also analyzed. Finally, the wireless biotelemetry function of the proposed antenna is realized and visualized by adopting a pair of nRF24L01 wireless transceivers, and sustainable and stable wireless data transmission characteristics are shown at a high data rate of 2 Mb/s with up to 20-cm transmission distance.

I. INTRODUCTION

CHRONIC kidney disease (CKD) has been acknowledged as one of the leading causes of global mortality, and as of 2022, it is currently on the rise [1]. CKD is a life-changing disease affecting approximately 700 million world-wide, contributing to 4.6% of all deaths in 2017, including deaths caused by impaired kidney function [1], [2]. It is a progressive pathology that eventually manifests as end-stage kidney disease (ESKD) or kidney failure. At this point, there is an irreversible decline in kidney function, leading to a high mortality rate even when employing optimal renal replacement therapy (RRT) [3]. RRT consists of hemodialysis (HD), peritoneal dialysis, and renal transplantation, with HD having a higher prevalence [4]. When performing HD, a conduit connection is made to access a large bore blood vessel through a surgical procedure known as vascular access (VA). The dominant types of VA used for HD are arteriovenous graft (AVG) and arteriovenous fistula (AVF). For both of these approaches, a connection will be made between the artery and vein directly in AVF, or through a synthetic tube, usually expanded polytetrafluoroethylene (ePTFE), in AVG. This allows blood to be exchanged within a dialyzer where toxins and waste products can be filtered, removed, and cleaned before the blood is returned to the patient.

Consequently, blood can enter the dialysis machine by artery and return to the patient through a vein [5]. However, repeated monitoring and surveillance of blood flow through the AVF or AVG are required for effective dialysis. Blood flow often becomes restricted due to a buildup of cellular tissue termed stenosis and/or forms a blood clot—thrombosis [6]. In addition, a significant cause of VA failure is intimal hyperplasia, which, through an inflammatory cascade, causes a blocking of the VA; this is initiated by endothelial injury. This wound response often occurs where the native vessel joins the synthetic prosthesis, called the anastomosis site [7]. In particular, VA failure accounts for at least 25% of all hospital stays and 50% of all patient care costs in the first year of dialysis [8], [9]. The frequency and unpredictability of VA failure can result in additional medical complications and significant financial burdens for treatment facilities. Regaining
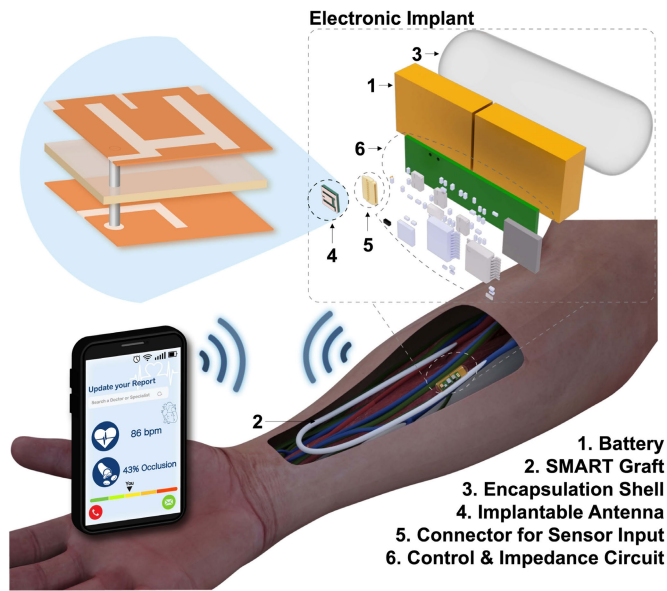
Fig. 1. Overview of the smart AVG and its detailed architecture.

access after thrombosis is generally more difficult and costly than intervening before thrombosis occurs [10].

A potential solution is a biosensor-integrated telemetric AVG, targeted at wireless detection and monitoring of vascular complications, such as stenosis and graft failure while maintaining functional access. The proposed SMART AVG is equipped with a multielectrode biosensor and wireless telemetry system for traditional HD and its complication detection. Fig. 1 illustrates the concept of the SMART wireless AVG, whereby the sensors can detect the changes occurring within the graft in situ and relay the data to the outside of the body. From this, the patient's AVG state can be monitored 24 h a day, providing the clinician with the most information for treatment planning. Therefore, this could allow the clinician to intervene early, possibly extending the length of the AVGs life, which, in turn, could result in better patient outcomes. Pertinent "smart vascular implants," such as self-reporting stents incorporating biosensors and telemetry systems, can detect cell growth, blood pressure, and blood flow in vessels, leading the way for a new generation of vascular intervention devices [11], [12], [13], [14], [15]. We, therefore, believe that this technology is also amenable to AVGs, which offers the potential for precision diagnosis and preemptive treatment for CKD patients.

Previously, our work has addressed the issues mentioned earlier in SMART stent technology and sensors [11], [16], [17]. However, a series of technical barriers exist in developing SMART AVGs, such as sensor design for discerning different cell types associated with stenosis, and thrombosis can cause issues while battery capacity and lifespan also pose problems. In addition, a low-power microcontroller that integrates programmable analog and high-speed wireless biotelemetry is given attention to deal with. With all these issues of the upmost concern, each subsystem becomes a bespoke task to create the overall device, which, finally, must all be integrated into a finished SMART AVG that

provides sound dialysis treatment with the benefits of remote monitoring.

In particular, one major hurdle associated with wireless AVGs is the design of efficient implantable antennas for bidirectional telemetry to guarantee wireless control and communication with the external device. In addition, implantable antennas encounter interdependent challenges in their design, including small size, wide bandwidth, sufficient gain, high radiation efficiency, and specific absorption rate (SAR) under the standard safety guidelines [18], [19], [20]. When designing an antenna, there is always a tradeoff between operating frequency and antenna performance. For example, low-frequency bands, such as the Medical Implant Communications Service (MICS) band (402–405 MHz) and the Medical Device Radio Communications Service (MedRadio) band (401–406, 413–419, 426–432, 438–444, and 451–457 MHz), have advantages of low power consumption due to the low penetration loss through biological tissues. On the other hand, higher frequency bands, such as the Wireless Medical Telemetry Service (WMTS) band (1.395–1.432 GHz) and the Industrial, Scientific, and Medical (ISM) band (433.05–434.79 MHz, 2.400–2.480 GHz, and 5.725–5.875 GHz), can lead to significant size reduction, wide bandwidth, and high data rates [21]. Therefore, selecting an appropriate frequency band under the condition of high loss and inhomogeneous human tissue is crucial for designing implantable antennas. To achieve high-speed data transfer and miniaturized self-reporting AVG, the 2.45-GHz ISM frequency band was selected as one operating frequency for the implantable antenna. In addition, the 1.4-GHz WMTS band was chosen for wireless power transfer.

Although, over the past few years, immense research has been devoted to antenna design for biomedical telemetry applications [22], [23], [24], [25], the majority of them are designed for deep implantable devices, such as leadless pacemakers [26], [27], deep brain stimulators [28], [29], and ingestible endoscopes [21], [30]. Specifically, only a few implantable antennas are targeted for the arm [31], [32], [33], [34], [35], [36], [37], [38] and none for internal implantation for HD applications. An early study of implantable antennas for arm-implanted wireless communication was reported by Xia et al. [31]; although the initial design size of this H-shaped cavity slot antenna is compact, the fabricated antenna is 2.5 times larger than the simulation one, which exhibits a gap between the simulation and the fabrication. Hossain et al. [32] proposed an implantable antenna for bidirectional communication between an external monitor and implants in the arm over the MICS band. This study, however, was constrained by the bulky volume of the antenna and insufficient bandwidth of 92.7 MHz, while the overall study lacks the analysis of the SAR, which is the top priority of wireless biomedical telemetry systems. With the rapid advancement in miniaturized multifunctional implantable medical devices (IMDs), multiple operations, such as wireless biotelemetry and wireless energy harvesting, are expected to be realized simultaneously with one single antenna. A dual-band cubic antenna loaded with four antenna elements has been developed in an arm model for wireless data telemetry and power transmission purposes. It exhibits superior bandwidths of 900 and 1500 MHz at

TABLE I
PROPOSED ANTENNA COMPARISON WITH PREVIOUS STUDIES IN ARM IMPLANTATION

Ref.	Year	Antenna Dimension (mm^3)	Antenna Type	Biotelemetry Validation in the System	Frequency (MHz)	Bandwidth (MHz)	Gain (dBi)	SAR (W/kg) 1-g	SAR (W/kg) 10-g
[31]	2009	2.8 × 4 × 1.6	Cavity Slot	No	2450	670	-26.5	0.0165^a	-
[32]	2015	40 × 30 × 1.525	Patch	No	404	92.7	-	-	-
[33]	2015	8.1 × 7.1 × 1.6	PIFA	No	2450	330	-12	5.2^b	-
[34]	2016	14 × 16 × 1.25	PIFA	No	402	33	-35.6	426.5	96.8
					915	46.9	-23.4	-	-
[35]	2019	28.85	Spiral Patch	No	915	768	-28	796.1	61.4
[36]	2020	9.5 × 9.5 × 0.635	Fractal	No	403	92	-28.1	-	47.9
					2440	320	-31.3	-	45.5
[37]	2020	15 × 15 × 15	Cubic	No	2450	900	-18.5	1101.7	-
					5800	1500		1135.8	-
[38]	2022	7.5 × 7.5 × 1.27	Patch	No	2450	680	-32.8	-	71.5
This work	2022	5 × 5 × 0.635	Patch	Yes	1400	300	-27.68	767	81.7
					2450	380	-27.10	785	84.6

^{a} The 1-g SAR was calculated from an input power of 25 µW
^{b} The 1-g SAR was calculated from an input power of 10 mW

2.45 and 5.8 GHz, respectively [36], but the maximum 1-g SAR values of 1101.7 and 1135.8 W/kg are high at both frequencies due to the employment of four antenna elements.

The proposed antenna is required to be designed with a small volume, low profile, and planar configuration linked to the host device architecture. Meanwhile, the antenna should exhibit wide bandwidth that supports strong communication ability while ensuring good radiation and patient safety. To this end, the simulations of the proposed antenna were carried out using a realistic human body model that included not only various tissues but also comprises of blood and a series of bones on the forearm. This low-profile antenna with dual-band functionality is miniaturized as an ideal applicant for the self-reporting AVG by etching two parallel notches and an H-like slot on the radiating patch, embedding an open-end slot in the ground, and a set of parameters analysis of the feed position, slot geometry, substrate material selection, and substrate thickness. Consequently, the proposed antenna with dual-band functionality has the smallest size of 15.875 mm^3 (5 × 5 × 0.635 mm^3) compared to other arm-implanted antennas in the literature, as shown in Table I. In addition, the proposed antenna can meet the requirement of a wide bandwidth at two resonant frequencies. It is worth noting that this study not only emphasizes the antenna design and tuning but also performs the validation on antenna biotelemetry performance from a system level, which is rare among all implantable antenna papers. The proposed antenna will realize the wireless data and power transmission of a self-reporting smart AVG operating at 2.45 and 1.4 GHz.

Initially, the antenna is conducted in a three-layer cubic phantom using ANSYS HFSS software. Then, the performance of the compact antenna is optimized by analyzing the feed position, substrate materials, substrate height, and the insertion of the ground slots, as shown in Section III. In addition, the proposed antenna is performed in a realistic human body model in a finite-difference time-domain (FDTD)-based Sim4life simulation. The SAR of the implantable antenna is
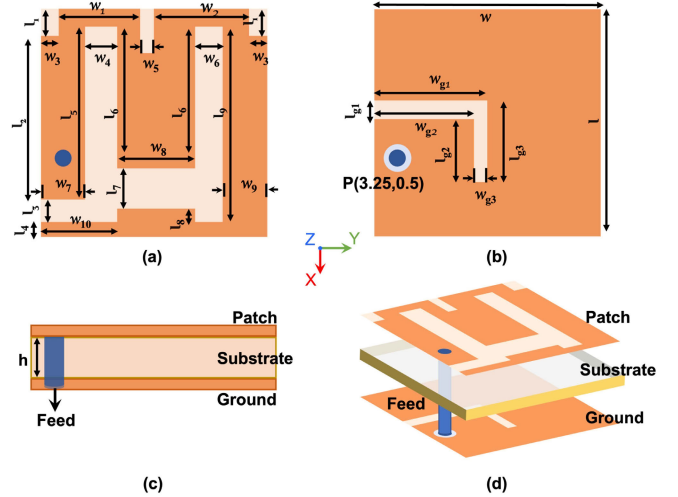

Fig. 2. Configuration of the proposed antenna with its design parameters. (a) Top view of the antenna. (b) Bottom view of the antenna. (c) Side view of the antenna. (d) Exploded view of the antenna.

simulated for calculations inside a human forearm model to prevent potential safety hazards. The measured results are evaluated in Section IV using pork mince. The effect of fat in the pork mince on the reflection coefficient of the antenna is also compared, illustrating that the frequency of the antenna is inversely proportional to the amount of fat in the tissue. In addition, a link budget for the proposed antenna is analyzed, while the practical demonstration of the wireless communication usability of the proposed antenna was conducted by adopting the nRF24L01 transceiver modules.

II. METHODOLOGY

A. Layout the Proposed Antenna

The proposed two-layer implantable antenna configuration is illustrated in Fig. 2(a)–(d). This miniaturized antenna is a

TABLE II
GEOMETRY PARAMETERS OF THE PROPOSED ANTENNA

Geometry parameter	Dimension (mm)	Geometry parameter	Dimension (mm)
w	5	w_1	1.8
l	5	w_2	2.1
h	0.635	w_3	0.4
l_1	0.6	w_4	0.7
l_2	3.6	w_5	0.3
l_3	0.5	w_6	0.6
l_4	0.3	w_7	1
l_5	3.8	w_8	1.7
l_6	3.1	w_9	1
l_7	0.9	w_{10}	1.7
l_8	0.3	w_{g1}	2.5
l_9	4.3	w_{g2}	2.2
l_{g1}	0.4	w_{g3}	0.3
l_{g2}	1.4		
l_{g3}	1.8		

Fig. 3. (a) Multilayer phantom simulation for the antenna simulation in HFSS. (b) Realistic human body "Glenn" model for the implantable antenna simulation in Sim4life; the implant is implanted between the radius and ulna approximately 2-cm distal from the radial tuberosity, thus avoiding impinging on the elbow joint. At a depth that is subcutaneously located over the brachioradialis and pronator teres in order to have minimal biological tissue obscuring the antenna, (c) anatomical position of the smart AVG implant and the comparison of the reflection coefficient ($|S_{11}|$) of the separate antenna simulation in the phantom in HFSS, the separate antenna simulation in the "Glenn" model in Sim4life, the entire AVG module simulation in the "Glenn" model in Sim4life, and the encapsulated AVG module simulation in "Glenn" in Sim4life.

meandered-shaped microstrip patch antenna with a low profile and is easy to integrate with the circuit, making it ideal for the AVG implant circuit. The radiating patch loaded with meandered slots is used to reduce the antenna size by increasing the physical path of the surface current flow. An L-shaped slot on the ground plane is responsible for the antenna tuning and bandwidth enhancement, as presented in Fig. 2(a)–(b), and the detailed parameters of the proposed antenna are presented in Table II. A coaxial feed with a diameter of 0.4 mm is located near the lower left corner of the patch antenna with a position of P (x = 3.25, y = 0.5), as annotated by the blue circle. To operate the miniaturized antenna at the desired resonant frequencies, we fabricated the proposed antenna on a Rogers RT/Duroid 6010 substrate (dielectric constant = 10.2 and tangent loss $\tan\delta$ = 0.0023) of 0.635 mm in thickness. This high-permittivity substrate reduces the antenna size by shortening the effective wavelength of the antenna. The final antenna was designed to have a compact volume of 15.875 mm³ (5 × 5 × 0.635 mm³), occupying a small implantation space in the body.

B. Simulation Environment

The antenna design and simulation setup were initially performed in Ansys HFSS version 2021 R1. According to the HD application, it needs to be able to be embedded inside the muscle tissue, and therefore, a three-layer tissue scenario—skin, fat, and muscle—is constructed with depths of 1.5, 8.5, and 52 mm, respectively, with a total depth of 62 mm; this is similar to previous modeling within an arm for dielectric materials [39] accounting for this. Fig. 3 illustrates how the proposed dual-band antenna is performed inside a phantom of dimensions 100 mm × 100 mm × 62 mm. The cube phantom box is assigned the corresponding dielectric properties of each tissue and is simulated in a radiation box with dimensions 500 mm × 500 mm × 500 mm. The electrical properties of different specific body tissues at frequencies of 1.4 and 2.45 GHz are shown in Table III.

Considering that the human body is not homogeneous, we then further assessed the performance of the antenna in a realistic human body model in FDTD-based Sim4Life
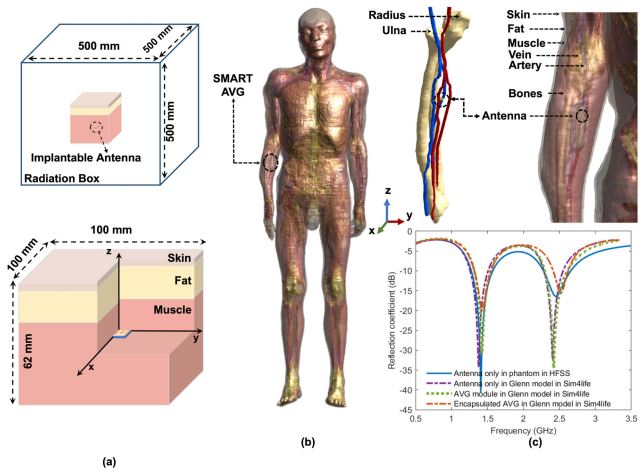
TABLE III
ELECTRICAL PROPERTIES OF THE BODY TISSUES AT THE DUAL-BAND

Electrical properties	Relative Permittivity ε_r		Conductivity $\sigma\Delta$ (S/m)	
Frequency (GHz)	1.4 GHz	2.45 GHz	1.4 GHz	2.45 GHz
Skin	39.66	38.00	1.03	1.46
Fat	11.15	10.82	0.14	0.26
Muscle	54.11	52.72	1.14	1.73
Blood	60.12	58.26	1.79	2.54
Bone (Cancellous)	19.90	18.54	0.46	0.80
Bone (Cortical)	12.05	11.38	0.21	0.39
Bone Marrow (Yellow)	5.42	5.29	0.05	0.09

software. Since the majority of CKD cases occur in elderly individuals, it is estimated that, in more than 50% of people over the age of 75 [40], [41], we set out the antenna analysis in the "Glenn" model, which is reconstructed from real-world human imaging data (Model information, Glenn, elderly, 84-year old, 1.73-m height, 61.1-cm weight, and 20.4-kg/m² BMI). The high-resolution "Glenn" model has a volume of 141.72 × 416.31 × 1624.62 mm³ and contains more than 300 tissues and organs throughout the entire body. It is an anatomical model created from real-human magnetic resonance image data, presenting a higher level of detail and accuracy than the phantom in HFSS. For the HD application, the antenna along with other components is implanted inside the muscle, at the center of the antebrachial location, between the artery and vein, as exhibited in Fig. 3(b) and (c). The proposed antenna is placed at a distance of 46 mm from the
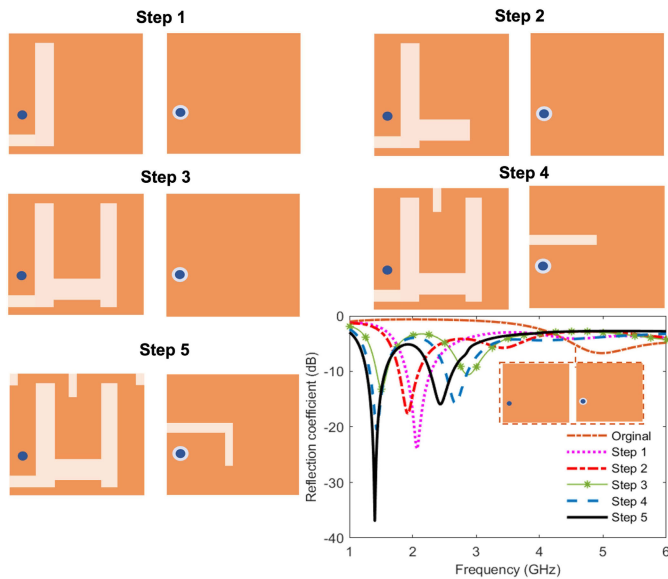
Fig. 4. Design process of the dual-band implantable antenna with the corresponding reflection coefficient of each design step.
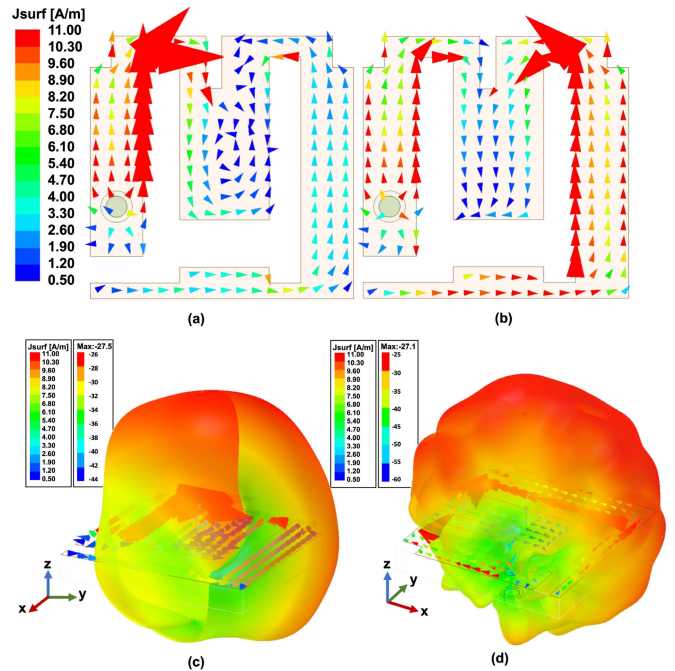

Fig. 5. Surface current distributions on the radiating patch at (a) 1.4 and (b) 2.45 GHz. Surface current distribution and 3-D far-field radiation pattern plots at (c) 1.4 and (d) 2.45 GHz.

outer portion of the arm. Fig. 3(c) also compares the reflection coefficient ($|S_{11}|$) of the proposed antenna in the phantom in HFSS and Sim4life, the entire smart AVG device simulated in the "Glenn" model, and the smart AVG encapsulated in biocompatible polydimethylsiloxane (PDMS: relative permittivity $\varepsilon_r = 2.76$ and tangent loss $\tan\delta = 0.03$) shell [42].

The difference of $|S_{11}|$ is observed between the HFSS and Sim4life simulation. This may be caused by the volume variance of the models and the contacting environment, where the antenna/smart AVG is surrounded by veins and arteries, in which blood has higher relative permittivity than the muscle. There is no significant deviation from the resonance frequencies and reflection coefficients of the simulations in sim4life except for the case of adding the encapsulation shell.

Fig. 3(c) shows that the addition of the biocompatible encapsulation shell can shift the two resonance frequencies to higher ones and affect the S_{11} values of the antenna, but the proposed antenna still exhibits robust performance at the target frequencies, with an S_{11} value of -18.86 dB at 1.4 GHz and -13.75-dB S_{11} at 2.45 GHz. The results also indicate the reliability of the phantom model used in HFSS, which will serve as a reference for antenna measurement validation.

C. Dual-Band Antenna Design

The miniaturized slot microstrip patch antenna that we designed has dual-band characteristics for biotelemetry purposes. To reduce the size of the antenna, a high relative permittivity material is employed as the substrate of the antenna. In addition, loading the meandered-shape and open-ended slots on the radiating element and ground plane will also effectively miniaturize the size while realizing dual-band characteristics [43]. The design and modification processes are visualized in Fig. 4, with the corresponding reflection coefficient at each step. Primarily, an L-like open-ended meandered slot was introduced to the radiating patch, which is

responsible for decreasing the resonant frequency by extending the current path within the patch. As presented in Fig. 4, the resonant frequency immediately dropped from 5 to 2.06 GHz, achieving over 50% miniaturization. In step 2, a horizontal rectangular slot is fused to radiating patch layer, resulting in frequency reduction and another slight resonance generated at around 3.5 GHz. U-slot patch antennas have been proposed and extensively used to obtain dual resonances with wide bandwidth characteristics [43], [44]. Therefore, we cut a U-like slot in the patch, by positioning each segment properly with the optimized dimensions in step 3. The antenna generated two resonances at 1.51 and 2.87 GHz with good impedance matching. To further reduce these two resonances to the desired bands (1.4 and 2.45 GHz), we employed a rectangular notch in the radiating patch and an open-ended slot near the feed location of the ground plane. Consequently, both frequencies moved to lower resonances in step 4, with better resonant characteristics for both bands. A further ground slot and two corner notches in radiating patch participate in the miniaturization and impedance matching of the antenna in step 5. The ground slots introduce an additional parasitic element, which contributes to the enhancement of radiation efficiency. It is obvious that the miniaturized dual-band antenna was successfully obtained by loading meandered slots in the radiator and the ground plane of a rectangular patch antenna. It is noteworthy that the optimal dimensions and locations of these slots and the feed were selected by analyzing the parametric studies in Section III.

D. Current Distribution

Current distributions of the proposed antenna on the radiating patch at 1.4 and 2.45 GHz are shown in Fig. 5(a). Current is pumped in from the power source through an SMA cable

into the inner conductor of the coaxial feed, which penetrates the substrate and connects the patch directly. Following this configuration, the current propagates from the feed line to the rest of the patch. The current distribution has the highest magnitude and strongly concentrates along the edges of the left arm at 1.4 GHz. In the contrast, the current distribution at 2.45 GHz shows a higher current density around the right arm. In addition, more significant charge accumulations can be seen at the edges of the patch and the two arms of the antenna at 2.45 GHz. The surface current distribution on an antenna affects the direction, efficiency, and polarization of the radiated wave, which together determines the antenna's radiation pattern. For example, the surface current distribution determines the direction of maximum radiation or the main lobe of the radiation pattern. The direction of maximum radiation is perpendicular to the direction of maximum surface current. As shown in Fig. 5(b) and (c), the maximum radiation occurs in close proximity to the maximum current density at both frequencies. In addition, it is observed that the edge of the radiating patch at 2.45 GHz exhibits a higher current density than that at 1.4 GHz, resulting a higher level of side lobes in the radiation pattern at 2.45 GHz.

E. SAR Distribution

Due to the effects of radiation interacting with the human body, it is necessary to consider SAR. SAR generally evaluates the rate of electromagnetic power absorbed by biological tissues (per unit mass) when exposed to the electromagnetic field and is determined by the following equation [45], [46]:

$$SAR = \frac{\sigma E^2}{2\rho} \tag{1}$$

where E is the magnitude of the electric field, and σ and ρ are the conductivity and mass density of the biological tissue, respectively. To comply with safety guidelines, SAR cannot exceed 1.6 W/kg, over averaged any 1-g cubic tissue regulated by the IEEE C95.1-1999 standards [47] or 2 W/Kg per 10 g according to IEEE C95.1-2005 [48]. To study the radiation effect on the human body and meet the limitation of the regulations, the SAR is simulated and analyzed in the Glenn human model using Sim4life software, and Fig. 6 presents the SAR distributions in the surrounding tissues. By assuming that the net input power of the antenna is 1 W, the 1-g peak average SAR is 767 and 785 W/kg observed at 1.4 and 2.45 GHz, respectively. To satisfy the human safety regulation, the maximum allowable input power is 2.08 and 2.03 mW over a 1-g SAR body model, correspondingly. The detailed SAR and maximum allowable input power for 1 and 10 g of tissues are shown in Table IV.

III. PARAMETRIC STUDIES

Parametric analysis is a crucial tool for antenna design, optimization, and fine-tuning. This section investigates a series of parametric studies aiming to realize a compact implantable antenna with outstanding antenna performance parameters in the WMTS and ISM bands. Several critical physical parameters, including feed positioning, slot dimensions, and substrate
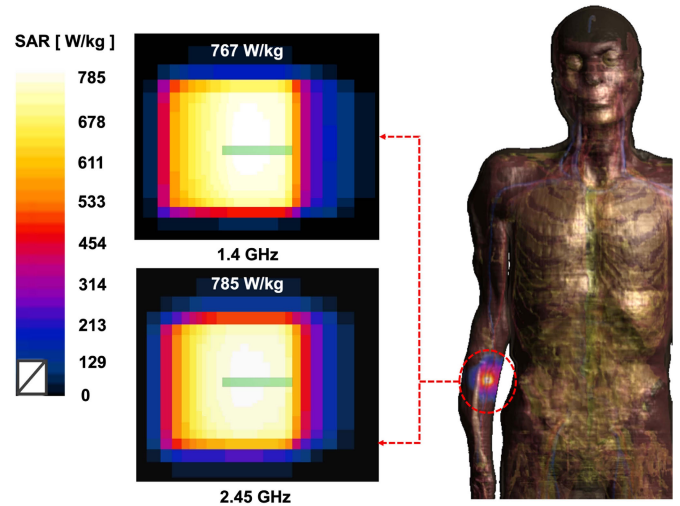

Fig. 6. Average SAR distribution of the implantable antenna inside the human forearm.

TABLE IV
PEAK AVERAGE SAR AND MAXIMUM ALLOWABLE NET-INPUT POWER FOR THE PROPOSED ANTENNA

Frequency (GHz)	Max-SAR (W/kg)		Max net input power (mW)	
	1-g	10-g	1-g	10-g
1.4 GHz	767	81.7	2.08	24.47
2.45 GHz	785	84.6	2.03	23.64
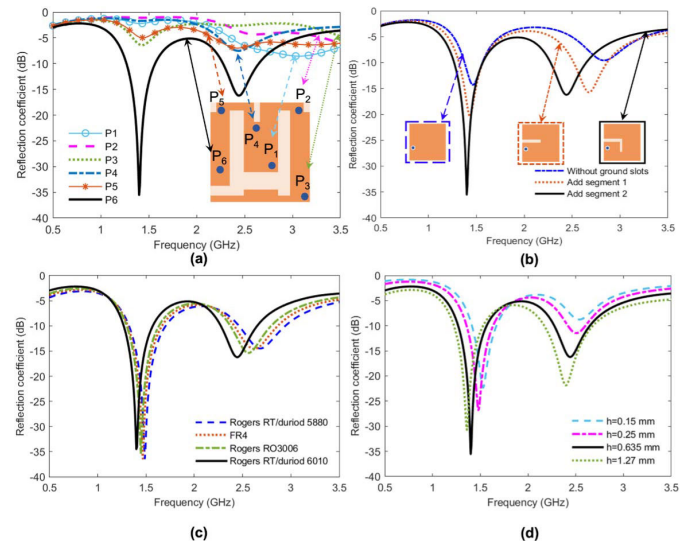
Fig. 7. Parametric studies of the proposed antenna with (a) feed position, (b) ground slots, (c) substrate materials, and (d) thickness of the substrate.

thickness, are explored, as well as the variation of the substrate materials, which affect the gain of the antenna.

A. Effect of Feed Locations

In a microstrip antenna, the input impedance varies with the position of the coaxial feed. Therefore, the feed position determines the input impedance or impedance matching between the transmission line and the port. The effect on

S_{11} of the antenna concerning the feed positions is shown in Fig. 7(a); there is no significant deviation from the resonance frequencies, but the S_{11} values and the antenna impedances are seriously affected by the feeding position. The initial two positions, $P_1(3,3)$ and $P_2(0.4,4.5)$, show no resonance in either frequency, while a single resonance is induced at 1.4 GHz by exciting the antenna at $P_3(4.6,4.6)$. Another single resonance appears at 2.43 GHz by placing the feed position at $P_4(1.5,2.3)$. A dual-band mode, with weak resonance characteristics, appears when the antenna is switched to $P_5(0.5,0.5)$. In addition, the impedance matching improved significantly at both resonant frequencies of 1.4 and 2.45 GHz when the feeding position changes to $P_6(3.25,0.5)$, which was adopted for the antenna design.

B. Effect of L-Shaped Ground Slot

As visualized in Fig. 2(b), an open-ended L-shaped ground slot is embedded in the antenna for compactness purposes. The slot consists of two segments, and their effect on the reflection coefficient is illustrated in Fig. 7(b). The incorporation of the ground slot enlarges the current path of the proposed antenna in the ground plane. By inserting slot segment 1, the resonant frequencies of both bands shifted to lower frequencies. When slot segment 2 is embedded on the ground plane, the ISM band exhibits a more significant reduction in resonance, while the lower band reduces only slightly. In the meantime, slot segment 2 significantly improved the impendence matching in the lower band. Overall, the slotted ground enhances the bandwidth of the antenna.

C. Effect of Substrate Materials

Appropriate selection of substrate material is critical in designing small dimensional antennas, especially at high operating frequencies. Four different commercial substrates with dielectric constants ranging from the values of 2.2 to 10.2—Rogers RT Duroid 5880, RO 3006, RT 6010, and FR4—have been considered for the proposed antenna. The following performance parameters—resonant frequency, return loss, peak gain, directivity, and bandwidth of different substrate materials—were compared under the same dimensions ($w = 5$ mm, $l = 5$ mm, and $h = 0.635$ mm), as exhibited in Fig. 7(c) and Table V. It can be observed that the substrate material with a higher value of permittivity exhibits lower resonant frequencies. The guided wavelength of the patch antenna can be reduced by using a high-permittivity substrate, thereby reducing its physical dimensions. In addition, the performance of peak gain and directivity also depends upon the substrate materials. Table V illustrates that both frequencies obtain the highest peak gains and peak directivities when the antenna is mounted on the Rogers RT/Duroid 6010 substrates. In addition, we further investigate the effect of loss tangent changes on the antenna. We set loss tangent values to 0.0001, 0.001, 0.0023, and 0.1 on the same Rogers RT/Duroid 6010 substrate. As depicted in Table VI, as the loss tangent increases, the gain decreases. Therefore, substrates with low loss tangent values are desired, where the Rogers RT/Duroid 6010 substrate has

TABLE V
SUBSTRATE PARAMETERS AND THEIR EFFECTS
ON THE PROPOSED ANTENNA

Substrate Material	ε_r	tanδ	Peak Gain (dB)	Peak Directivity (dB)
Rogers RT 5880	2.2	0.004	-27.97[a] -27.57[b]	3.59[a] 6.70[b]
FR4	4.4	0.01	-27.88[a] -27.62[b]	3.64[a] 6.79[b]
Rogers RO 3006	6.15	0.0025	-27.79[a] -27.58[b]	3.68[a] 6.87[b]
Rogers RT 6010	10.2	0.0023	-27.68[a] -27.10[b]	3.75[a] 7.06[b]

[a] at 1.4 GHz
[b] at 2.45 GHz

the lowest loss tangent value among the four substrates listed in Table V.

D. Effect of Substrate Thickness

To explore the appropriate substrate thickness for the proposed antenna, we compared how it performed with varying substrate thicknesses (h) ranging from 0.15 to 1.27 mm. Fig. 7(d) shows the values of S_{11} corresponding to the substrate thicknesses in a given Rogers RT/duroid 6010LM material, proving that the resonant frequencies decrease by increasing the height of the substrate. Notably, a higher thickness leads to wider bandwidth and a lower reflection coefficient, which is desired. Generally, the magnitude of the fringing field generated between the periphery patch and the ground plane is responsible for the radiation of the antenna, and it depends on the width of the antenna and the height of the substrate. As the substrate thickness increases, the parasitic capacitance formed by the fringing fields also increases, leading to the effect of shifting the resonance frequency to lower values [49]. As expected, Fig. 7(d) shows that, as the thickness of the substrate increases, the resonance frequency decreases, but the bandwidth increases. Considering the above, we chose the 0.635 mm height to achieve a sufficient bandwidth for biomedical wireless communication and the required device compactness (bandwidths of 300 MHz at 1.4 GHz and 380 MHz at 2.45 GHz).

IV. EXPERIMENTAL SETUP AND MEASUREMENT

After the antenna was analyzed in different simulation scenarios, it was time to investigate the actual performance in vitro. The physical antenna prototypes were fabricated, and a series of measurements were performed. For simplicity, a muscle model (mixed with blood and fat) with a dimension of $100 \times 100 \times 60$ mm^3 was used for the measurement. The results were compared with the simulated version of the homogenous phantom.

The fabricated prototype is shown in Fig. 8(a). To excite the antenna, a 50-Ω coaxial cable is used to feed the antenna, and
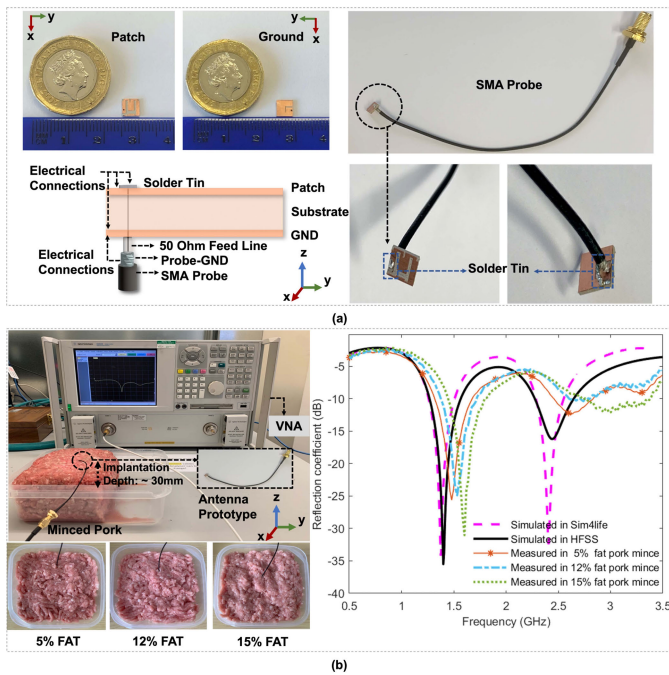
Fig. 8. (a) Fabricated antenna prototype and solder details. (b) Reflection coefficient measurement setup and results for the proposed antenna with different fat percentages in the pork mince.

hence, the soldering procedure is significant for obtaining good impedance matching. The conductor within the insulation of the coaxial cable is soldered to the radiating metal patch, while the outer conductor is connected to the ground plane of the antenna. Then another end of the coaxial cable will be linked to a vector network analyzer (VNA, Agilent Technologies E83628) for measuring the S-parameters of the antenna.

A. Reflection Coefficient for the Implantable Antenna

The measurement setup of the reflection coefficient for the proposed antenna is presented in Fig. 8(b). The resonant frequency of the antenna is highly dependent on the various dielectric properties of different tissues [50]. Since the antenna is placed in the muscle tissue layer in the simulation, we employed pork mince for the measurement. We studied three pork minces with different fat percentages: 5% fat, 12% fat, and 15% fat.

A comparison between the experimental and simulated reflection coefficients is visualized in Fig. 8(b). In particular, the measured antenna bandwidths of reflection coefficient are below −10 dB, ranging from 1.31 to 1.68 GHz (370 MHz) and from 2.44 to 2.83 GHz (390 MHz) in the pork mince with 5% fat, which can cover the desired frequency bands. However, the resonant frequencies shift to higher values compared with the simulation (HFSS) results, which may be on account of the existence of the fat tissue and the air gaps among the tissues [51]. In addition, the result reveals that the higher the fat content in the pork mince, the greater the shift in the resonance frequencies; more particularly, the low relative permittivity and conductivity of fat tissue will decrease the electrical properties of the environment. Consequently, the
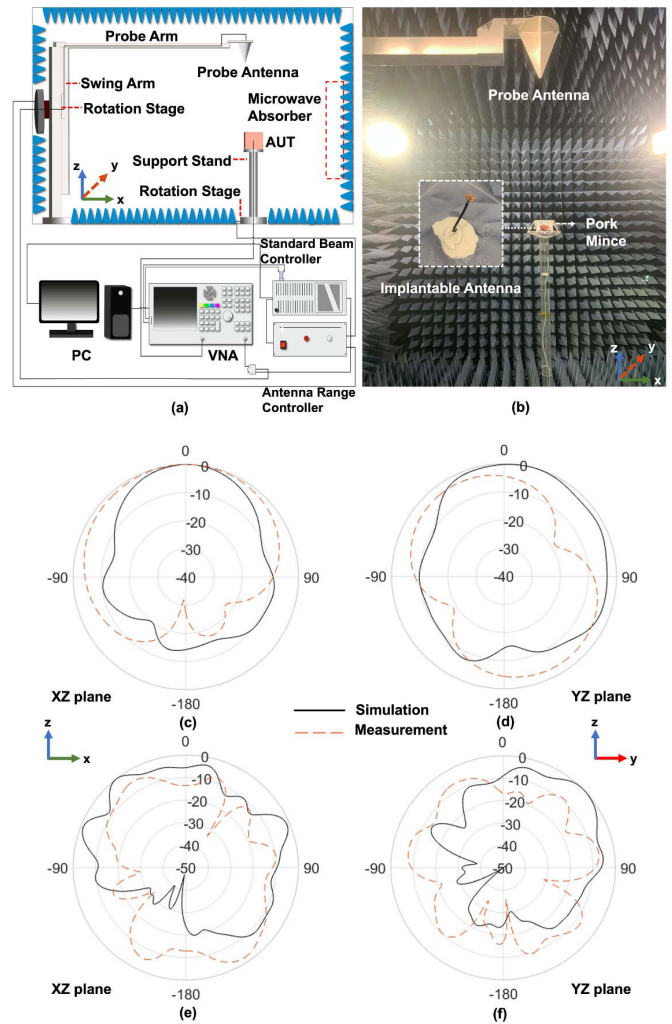

Fig. 9. (a) Schematic of an anechoic chamber and its relevant hardware. (b) Far-field radiation pattern measurement setup. (c)–(f) Comparison normalized radiation pattern (in dB) between the simulation and measurement results at (c) E-plane at 1.4 GHz, (d) H-plane at 1.4 GHz, (e) E-plane at 2.45 GHz, and (f) H-plane at 2.45 GHz.

antenna in the pork mince with 5% fat shows good agreement with the simulation result.

B. Radiation Pattern Measurement

Far-field radiation pattern and gain are the key factors to guarantee reliable data communication, which can be measured in an anechoic chamber. Fig. 9(a) presents a schematic of an anechoic chamber and its relevant hardware setup. Notably, this measurement system uses a "theta over phi" (θ/ϕ) coordinate system, which indicates that the azimuth is scanned by rotation of θ and elevation is scanned by rotation of ϕ. The measurement setup in the anechoic chamber is demonstrated in Fig. 9(b). To accurately measure the antenna under test (AUT), the AUT is placed in the center of the support stand at a 1.16 m distance from the probe antenna, while the implantable antenna is inserted into the pork mince through the bottom hole of the measuring box, connecting directly to the coaxial feed cable in the support stand to mitigate the effect of the metal exposure of the cable. Absorption foam is added to the bottom of the

measuring box to further combat interference. The comparison of simulated and measured normalized radiation patterns in the E-plane and the H-plane at 1.4 and 2.45 GHz is exhibited in Fig. 9(c)–(f), respectively. The measurement results at 1.4 and 2.45 GHz, on the E-plane, are closely consistent with the simulated ones. For the H-plane, the measured radiation patterns show suitable agreement with the simulated other than the orientation differences between them. This may be due to the misalignment of the antenna placement in the pork mince during the rotation of the support stand. In addition, the peak gains of the antenna measured in the pork mince phantom are −31.5 and −32.1 dBi at 2.45 and 1.4 GHz, respectively. The deviation between the simulated and measured gain might be caused by the following reasons.

1) The antenna was inserted into the pork mince but not fixed in one place during the radiation pattern measurement. Thus, the orientation of the antenna might be changed due to the movement of the rotation stage.

2) The implantation depth of the antenna also determines the gain of the antennas. Fig. 9(b) presents the setup of the radiation pattern measurement; the proposed antenna with a short coaxial cable (to reduce cable loss) is connected to another coaxial cable through the bottom of the container (to mitigate the influence of the metal exposure) in the support stand, resulting in a deeper implant position compared to the simulation. In addition, the reflection from the container/box can affect the performance of the antenna gain values.

3) The contacting environment of the antenna is another key factor affecting its performance. Therefore, the space/air gap in the minced pork can also influence the antenna gain.

In addition, considering the fact that the antenna will be surrounded by heterogeneous tissues, we further performed 3-D far-field radiation pattern simulations at 1.4 and 2.45 GHz in the anatomical human phantom "Glenn" in Sim4Life. As shown in Fig. 10, the proposed antenna emits high-strength radiation from Glenn's arm to the outside of the body, which facilitates wireless biotelemetry with the exterior device. As aforementioned, the antenna is placed centrally in the forearm, between the artery and vein, 46 mm subcutaneously on the outside of the arm. The peak gains of −31.1 and −29.33 dBi are obtained at 1.4 and 2.45 GHz, respectively. Compared to the simulation results in HFSS, the reduction of the peak gain values may be caused by the volume variance of the models and their surrounding environments, as previously mentioned in the $|S_{11}|$ comparison. In addition, the implantation position in the Glenn model is deeper than that of the three-layer phantom model distance from the antenna to the outer arm.

C. Wireless Link Budget Analysis

Link budget calculations are performed in this study to estimate the communication capability of the proposed implantable antenna with an external standard dipole antenna (as a reference). The proposed implantable and dipole antenna with a gain of 2.15 dBi are assumed as transmitter and receiver, respectively. To mitigate electromagnetic interference to the human body and ensure communication quality, the
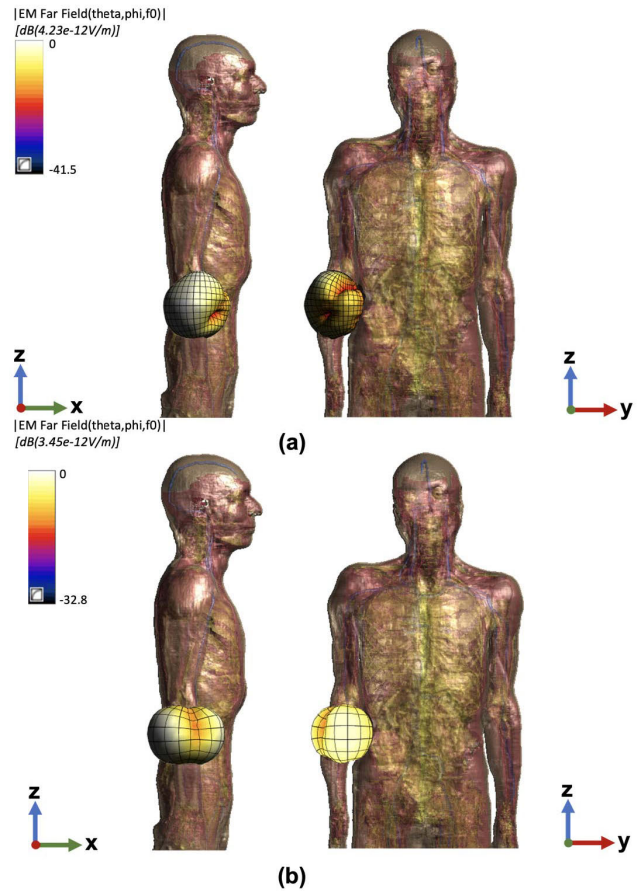

Fig. 10. 3-D radiation patterns of the proposed antenna in the realistic human model "Glenn" arm at (a) 1.4 and (b) 2.45 GHz.

TABLE VI
EFFECTS OF LOSS TANGENT VALUES ON THE PROPOSED ANTENNA GAIN

Loss tangent	Peak Gain (dB)	
tanδ	1.4 GHz	2.45 GHz
0.0001	-27.66	-27.092
0.01	-27.76	-27.094
0.0023	-27.68	-27.10
0.01	-27.70	-27.11
0.1	-27.94	-27.35

input power to the implantable antenna is set to 25 μW (−16 dBm) under the European Research Council limitation [52]. In addition, high data rates of 1 and 2 Mb/s are considered in the link budget analysis of this wireless smart AVG system to guarantee efficient communication with the external device. Other related parameters for calculation of the link budget concerning transmitter, receiver, propagation, and signal quality are presented in Table VII. Link margin (LM) in a wireless communication system can be computed, as described in the following [53], [54]:

$$LM(\text{dB}) = \frac{C_1}{N_o} - \frac{C_2}{N_o} \qquad (2)$$

$$\frac{C_1}{N_o} = P_t + G_t + G_r - L_f - N_o \qquad (3)$$

$$\frac{C_2}{N_o} = \frac{E_b}{N_o} + 10\log_{10}(B_r) - G_c + G_d \qquad (4)$$

TABLE VII
LINK BUDGET PARAMETERS FOR THE PROPOSED ANTENNA

| Transmitter (Implantable antenna)	
Operation frequency f_o (GHz)	2.45
Transmitter power P_t (dBW)	-46
Transmitter antenna gain G_t (dBi)	-27.10
Receiver	
Receiver antenna gain G_r (dBi)	2.15
Boltzmann constant (k)	1.38×10^{-23}
Temperature T_o (K)	293
Receiver-NF (dB)	2.5
Noise power density N_o (dB/Hz)	-201.7
Propagation	
Distance (m)	1–10
Free pace loss (L_f) (dB)	Distance dependent
Signal Quality	
Bit rate B_r (Mbps)	1 / 2
Bit error rate	1.0×10^{-5}
E_b/N_o (ideal PSK) (dB)	9.6
Coding Gain G_c (dB)	0
Fixing Deterioration G_d (dB)	2.5
Link Margin (dB)	
$LM = A_l - R_l$	
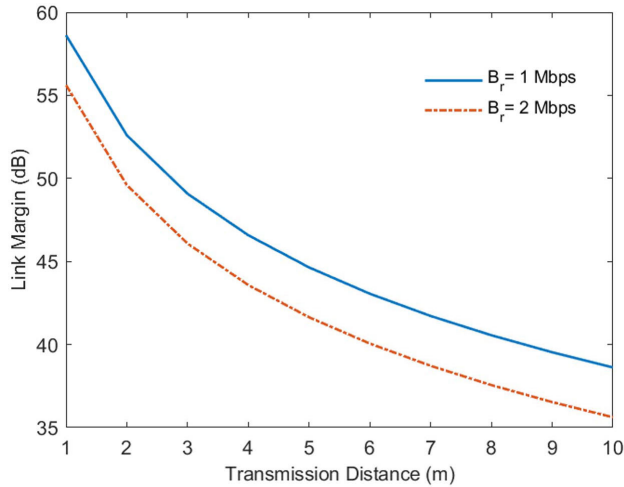
Fig. 11.   Calculated LM as a function of distance at 1- and 2-Mb/s data rates.

$$L_f = 20 \log_{10} \left(\frac{4\pi d}{\lambda} \right) \tag{5}$$

$$N_o = 10 \log_{10}(k) + 10 \log_{10}(T_i) \tag{6}$$

$$T_i = T_0 (NF - 1) \tag{7}$$

where (C_1/N_o) is the signal-to-noise ratio for the actual link (A_l) of the implantable antenna and (C_2/N_o) is the signal-to-noise ratio of the required link (R_l).

The computed LM of the proposed antenna for various transmission distances at different data rates is shown in Fig. 11, which shows that the implantable antenna can easily achieve 2 Mb/s of data rate within a distance of 10 m. As the external receiver will be in contact with the skin, the wireless data transmission distance should be less than 5 cm. As shown in Fig. 11, the LM is higher than 55 dB within 1 m, which is sufficient for the wireless biotelemetry of the proposed antenna.

Furthermore, wireless data transmission is experimentally validated in Fig. 12, where the transmitter module equipped
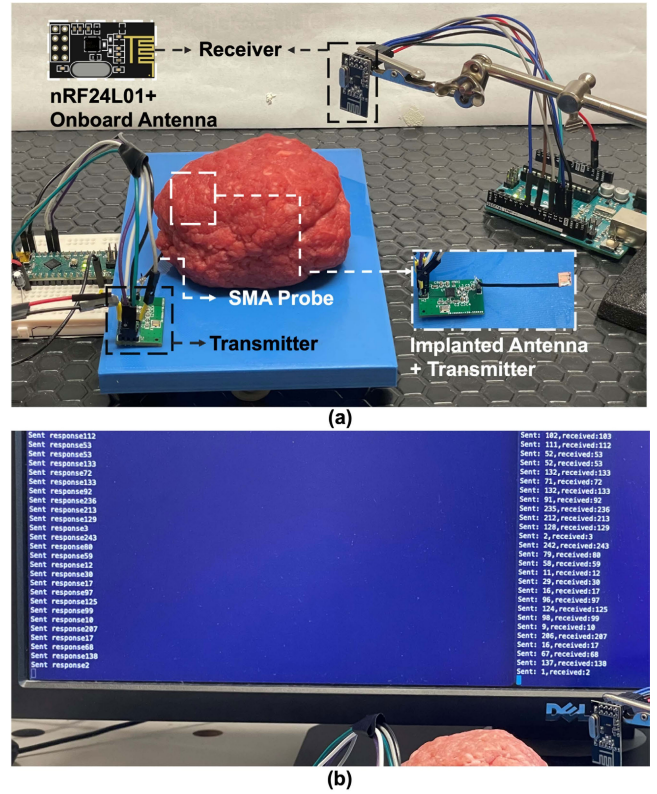

Fig. 12.   (a) Wireless data transmission scenario setup. (b) Results of the output on Arduino serial monitor: transmitter monitor (left) and receiver monitor (right).

with the proposed implantable antenna can steadily and continuously transfer and receive data at a distance of 20 cm.

D. Wireless Data Transmission Validation

Prior to integrating the proposed antenna on the AV graft implant, it is required to demonstrate the actual feasibility of data transfer for the implantable antenna. Consequently, this study employs an ultralow power consumption protocol nRF24L01 with a proprietary adaptive network technology (ANT) for both transmitter and receiver circuits for the wireless biotelemetry system. In particular, the nRF24L01 module serves the ISM frequency band (2.400–2.480 GHz) by adopting the Gaussian frequency-shift keying modulation. It offers a maximum of 2-Mb/s data transmission rate, which can transmit data efficiently. Fig. 12 illustrates the communication scenario under which data are being transmitted from a transmitter in-body (minced pork) to an exterior receiver. To verify the performance of the proposed antenna, we modified and fabricated a new PCB for the transmitter module based on the nRF24L01 module and directly connect the implantable antenna (i.e., proposed antenna) enclosed by minced pork, while the receiver module adopts the commercial nRF24L01 receiver with an onboard antenna. The receiving antenna in the nRF24L01 module follows an inverted F-shaped design to obtain the compact structure, and it can operate in the range of 2.4–2.525 GHz with high precision. Subsequently, the transceiver modules interface with microcontrollers for transmitting and receiving a set of random data, respectively.

In particular, this pair of transceivers operates at 2.45 GHz, aiming to support bidirectional data transmission for wireless smart AVG. Consequently, the transmitter module equipped with the proposed implantable antenna can steadily and continuously transfer and receive data at a distance of 20 cm. We did not explore or demonstrate higher transmission distances as this is adequate for targeted implantation applications. In addition, we did not account for the tissue losses in the prior link budget calculation, and the actual arm contains less muscle compared to the measurement setup.

V. Conclusion and Future Work

This article presents a miniaturized implantable antenna operating at 1.4 and 2.45 GHz for wireless powering, biotelemetry, and purposes of self-reporting AVGs. The design process, parameter features, and corresponding propagation characteristics are reported in this study. In particular, the antenna performance was investigated by placing the antenna between the artery and vein in the antebrachial location (forearm) of a human body model, resembling the actual implantation site in vivo. The measured results were evaluated by performing the antenna prototypes inside the pork mince. Regardless of several effects on the antenna performance, including fat presence, coaxial cable loss, and orientation misalignment, the measured results show suitable performance. In addition, SAR values and the maximum allowed input power for the antenna were simulated in the human model. The computed LK indicated a redundant communication link that can be reached by employing the proposed implantable antenna and an external reference antenna. Moreover, the conducted demonstration of the wireless communication system visualizes that the proposed antenna is reliable and suitable for wireless data transmission in HD applications. These data support that this compact antenna is a good candidate for supporting the wireless telemetry of SMART AVGs. In the future, we will further implement the wireless power supply function of the antenna and develop the wireless system for SMART vascular active implants by considering both wireless power and data transmission.

References

[1] E. F. Carney, "The impact of chronic kidney disease on global health," *Nature Rev. Nephrol.*, vol. 16, no. 5, p. 251, May 2020.

[2] P. Cockwell and L.-A. Fisher, "The global burden of chronic kidney disease," *Lancet*, vol. 395, no. 10225, pp. 662–664, Feb. 2020.

[3] P. K. Moore, R. K. Hsu, and K. D. Liu, "Management of acute kidney injury: Core curriculum 2018," *Amer. J. Kidney Diseases*, vol. 72, no. 1, pp. 136–148, 2018.

[4] J. H. Lawson, L. E. Niklason, and P. Roy-Chaudhury, "Challenges and novel therapies for vascular access in haemodialysis," *Nature Rev. Nephrol.*, vol. 16, no. 10, pp. 586–602, Oct. 2020.

[5] D. Santoro et al., "Vascular access for hemodialysis: Current perspectives," *Int. J. Nephrol. Renovascular Disease*, vol. 7, p. 281, Jul. 2014.

[6] L. Kumbar, J. Karim, and A. Besarab, "Surveillance and monitoring of dialysis access," *Int. J. Nephrol.*, vol. 2012, Jan. 2012, Art. no. 649735.

[7] J. M. MacRae et al., "Arteriovenous access failure, stenosis, and thrombosis," *Can. J. Kidney Health Disease*, vol. 3, Sep. 2016, Art. no. 2054358116669126.

[8] C. A. Schinstock et al., "Outcomes of arteriovenous fistula creation after the fistula first initiative," *Clin. J. Amer. Soc. Nephrol.*, vol. 6, no. 8, pp. 1996–2002, 2011.

[9] R. Hakim and J. Himmelfarb, "Hemodialysis access failure: A call to action," *Kidney Int.*, vol. 54, no. 4, pp. 1029–1040, 1998.

[10] Y.-N. Wang et al., "Chronic kidney disease: Biomarker diagnosis to therapeutic targets," *Clinica Chim. Acta*, vol. 499, pp. 54–63, Dec. 2019.

[11] D. Hoare et al., "Predicting cardiovascular stent complications using self-reporting biosensors for noninvasive detection of disease," *Adv. Sci.*, vol. 9, no. 15, 2022, Art. no. 2105285.

[12] J. Vishnu and G. Manivasagam, "Perspectives on smart stents with sensors: From conventional permanent to novel bioabsorbable smart stent technologies," *Med. Devices Sensors*, vol. 3, no. 6, 2020, Art. no. e10116.

[13] A. Bussooa, S. Neale, and J. Mercer, "Future of smart cardiovascular implants," *Sensors*, vol. 18, no. 7, p. 2008, Jun. 2018.

[14] D. Hoare, A. Bussooa, S. Neale, N. Mirzai, and J. Mercer, "The future of cardiovascular stents: Bioresorbable and integrated biosensor technology," *Adv. Sci.*, vol. 6, no. 20, Oct. 2019, Art. no. 1900856.

[15] A. Molloy et al., "Challenges to the development of the next generation of self-reporting cardiovascular implantable medical devices," *IEEE Rev. Biomed. Eng.*, vol. 15, pp. 260–272, 2022.

[16] A. Bussooa et al., "Impedimetric detection and electromediated apoptosis of vascular smooth muscle using microfabricated biosensors for diagnosis and therapeutic intervention in cardiovascular diseases," *Adv. Sci.*, vol. 7, no. 18, Sep. 2020, Art. no. 1902999.

[17] D. Hoare et al., "An impedance sensor for pathologically relevant detection of in-stent restenosis in vitro," in *Proc. 44th Annu. Int. Conf. IEEE Eng. Med. Biol. Soc. (EMBC)*, Jul. 2022, pp. 2298–2301.

[18] J. Zhang, R. Das, J. Zhao, N. Mirzai, J. Mercer, and H. Heidari, "Battery-free and wireless technologies for cardiovascular implantable medical devices," *Adv. Mater. Technol.*, vol. 7, no. 6, 2022, Art. no. 2101086.

[19] B. D. Nelson, S. S. Karipott, Y. Wang, and K. G. Ong, "Wireless technologies for implantable devices," *Sensors*, vol. 20, no. 16, p. 4604, Aug. 2020.

[20] C. Liu, Y.-X. Guo, and S. Xiao, "A review of implantable antennas for wireless biomedical devices," in *Forum for Electromagnetic Research Methods and Application Technologies (FERMAT)*, vol. 14, no. 3. Orlando, FL, USA: Univ. of Central Florida, Department of Electrical Engineering and Computer Science—ECE Division, 2016, pp. 1–11.

[21] A. Kiourti, K. A. Psathas, and K. S. Nikita, "Implantable and ingestible medical devices with wireless telemetry functionalities: A review of current status and challenges," *Bioelectromagnetics*, vol. 35, no. 1, pp. 1–15, Jan. 2014.

[22] J. Zhao et al., "Self-powered implantable medical devices: Photovoltaic energy harvesting review," *Adv. Healthcare Mater.*, vol. 9, no. 17, 2020, Art. no. 2000779.

[23] G. Galeote-Checa, K. Uke, L. Sohail, R. Das, and H. Heidari, "Flexible wirelessly powered implantable device," in *Proc. 26th IEEE Int. Conf. Electron., Circuits Syst. (ICECS)*, Nov. 2019, pp. 891–894.

[24] J. Zhang et al., "Wireless impedance platform for autonomous vascular implantable devices," in *Proc. 29th IEEE Int. Conf. Electron., Circuits Syst. (ICECS)*, Oct. 2022, pp. 1–4.

[25] J. Zhang, R. Das, Q. H. Abbasi, N. Mirzai, J. Mercer, and H. Heidari, "Dual-band microstrip patch antenna for fully-wireless smart stent," in *Proc. IEEE Int. Symp. Antennas Propag. USNC-URSI Radio Sci. Meeting (APS/URSI)*, Dec. 2021, pp. 1035–1036.

[26] S. M. Asif, A. Iftikhar, B. D. Braaten, D. L. Ewert, and K. Maile, "A wide-band tissue numerical model for deeply implantable antennas for RF-powered leadless pacemakers," *IEEE Access*, vol. 7, pp. 31031–31042, 2019.

[27] M. Zada, I. A. Shah, A. Basir, and H. Yoo, "Ultra-compact implantable antenna with enhanced performance for leadless cardiac pacemaker system," *IEEE Trans. Antennas Propag.*, vol. 69, no. 2, pp. 1152–1157, Feb. 2020.

[28] S. Ma, T. Bjorninen, L. Sydanheimo, M. H. Voutilainen, and L. Ukkonen, "Double split rings as extremely small and tuneable antennas for brain implantable wireless medical microsystems," *IEEE Trans. Antennas Propag.*, vol. 69, no. 2, pp. 760–768, Feb. 2021.

[29] A. Burton et al., "Wireless, battery-free, and fully implantable electrical neurostimulation in freely moving rodents," *Microsyst. Nanoeng.*, vol. 7, no. 1, pp. 1–12, Aug. 2021.

[30] W. Cui, R. Liu, L. Wang, M. Wang, H. Zheng, and E. Li, "Design of wideband implantable antenna for wireless capsule endoscope system," *IEEE Antennas Wireless Propag. Lett.*, vol. 18, no. 12, pp. 2706–2710, Dec. 2019.

[31] W. Xia, K. Saito, M. Takahashi, and K. Ito, "Performances of an implanted cavity slot antenna embedded in the human arm," *IEEE Trans. Antennas Propag.*, vol. 57, no. 4, pp. 894–899, Apr. 2009.

[32] T. Hossain, R. Mahmud, H. K. Juhi, M. R. Imtiaz, and R. Hoque, "Design and performance analysis of a biomedical implantable patch antenna," in *Proc. Int. Conf. Adv. Electr. Eng. (ICAEE)*, Dec. 2015, pp. 47–50.

[33] F. Gozasht and A. S. Mohan, "Miniature implantable PIFA for telemetry in the ISM band: Design and link budget analysis," in *Proc. Int. Symp. Antennas Propag. (ISAP)*, Nov. 2015, pp. 1–4.

[34] S. Bakogianni and S. Koulouridis, "Design of a novel miniature implantable rectenna for in-body medical devices power support," in *Proc. 10th Eur. Conf. Antennas Propag. (EuCAP)*, Apr. 2016, pp. 1–5.

[35] A. Basir and H. Yoo, "A stable impedance-matched ultrawideband antenna system mitigating detuning effects for multiple biotelemetric applications," *IEEE Trans. Antennas Propag.*, vol. 67, no. 5, pp. 3416–3421, May 2019.

[36] Y. Fan, H. Liu, X. Liu, Y. Cao, Z. Li, and M. M. Tentzeris, "Novel coated differentially fed dual-band fractal antenna for implantable medical devices," *IET Microw., Antennas Propag.*, vol. 14, no. 2, pp. 199–208, 2020.

[37] V. Kaim, B. K. Kanaujia, and K. Rambabu, "Quadrilateral spatial diversity circularly polarized MIMO cubic implantable antenna system for biotelemetry," *IEEE Trans. Antennas Propag.*, vol. 69, no. 3, pp. 1260–1272, Mar. 2021.

[38] C. Xu, Y. Fan, and X. Liu, "A circularly polarized implantable rectenna for microwave wireless power transfer," *Micromachines*, vol. 13, no. 1, p. 121, 2022.

[39] K. Ito and Y. Hotta, "Signal path loss simulation of human arm for galvanic coupling intra-body communication using circuit and finite element method models," in *Proc. IEEE 12th Int. Symp. Auto. Decentralized Syst.*, Mar. 2015, pp. 230–235.

[40] C. Couchoud, O. Moranne, L. Frimat, M. Labeeuw, V. Allot, and B. Stengel, "Associations between comorbidities, treatment choice and outcome in the elderly with end-stage renal disease," *Nephrol. Dialysis Transplantation*, vol. 22, no. 11, pp. 3246–3254, 2007.

[41] H. Xu et al., "Kidney function, kidney function decline, and the risk of dementia in older adults: A registry-based study," *Neurology*, vol. 96, no. 24, pp. e2956–e2965, 2021.

[42] J. Trajkovikj, J.-F. Zürcher, and A. K. Skrivervik, "PDMS, a robust casing for flexible W-ban antennas [EurAAP corner]," *IEEE Antennas Propag. Mag.*, vol. 55, no. 5, pp. 287–297, Oct. 2013.

[43] M. U. Khan, M. S. Sharawi, and R. Mittra, "Microstrip patch antenna miniaturisation techniques: A review," *IET Microw., Antennas Propag.*, vol. 9, no. 9, pp. 913–922, 2015.

[44] S. Weigand, G. H. Huff, K. H. Pan, and J. T. Bernhard, "Analysis and design of broad-band single-layer rectangular U-slot microstrip patch antennas," *IEEE Trans. Antennas Propag.*, vol. 51, no. 3, pp. 457–468, Mar. 2003.

[45] S. Liu, S.-S. Qi, W. Wu, and D.-G. Fang, "Single-layer single-patch four-band asymmetrical U-slot patch antenna," *IEEE Trans. Antennas Propag.*, vol. 62, no. 9, pp. 4895–4899, Sep. 2014.

[46] D. T. Le, L. Hamada, S. Watanabe, and T. Onishi, "A fast estimation technique for evaluating the specific absorption rate of multiple-antenna transmitting devices," *IEEE Trans. Antennas Propag.*, vol. 65, no. 4, pp. 1947–1957, Apr. 2017.

[47] D. J. Panagopoulos, O. Johansson, and G. L. Carlo, "Evaluation of specific absorption rate as a dosimetric quantity for electromagnetic fields bioeffects," *PLoS ONE*, vol. 8, no. 6, Jun. 2013, Art. no. e62663.

[48] *IEEE Standard for Safety Levels With Respect to Human Exposure to Radio Frequency Electromagnetic Fields, 3kHz to 300GHz*, Standard C95. 1-1991, IEEE Standards Coordinating Committee, 1992.

[49] A. Hirata and O. Fujiwara, "The correlation between mass-averaged SAR and temperature elevation in the human head model exposed to RF near-fields from 1 to 6 GHz," *Phys. Med. Biol.*, vol. 54, no. 23, pp. 7227–7238, Dec. 2009.

[50] J. Dahele and K. Lee, "Effect of substrate thickness on the performance of a circular-disk microstrip antenna," *IEEE Trans. Antennas Propag.*, vol. AP-31, no. 2, pp. 358–360, Mar. 1983.

[51] M. K. Magill, G. A. Conway, and W. G. Scanlon, "Tissue-independent implantable antenna for in-body communications at 2.36–2.5 GHz," *IEEE Trans. Antennas Propag.*, vol. 65, no. 9, pp. 4406–4417, Sep. 2017.

[52] D. Negi, R. Khanna, and J. Kaur, "Design and performance analysis of a conformal CPW fed wideband antenna with mu-negative metamaterial for wearable applications," *Int. J. Microw. Wireless Technol.*, vol. 11, no. 8, pp. 806–820, Oct. 2019.

[53] H. Mizuno, M. Takahashi, K. Saito, and K. Ito, "Development of an implanted helical folded dipole antenna for 2.45 GHz applications," in *Proc. Int. Workshop Antenna Technol. (iWAT)*, Mar. 2010, pp. 1–4.

[54] R. Das and H. Yoo, "A wideband circularly polarized conformal endoscopic antenna system for high-speed data transfer," *IEEE Trans. Antennas Propag.*, vol. 65, no. 6, pp. 2816–2826, Jun. 2017.

[55] X. Y. Liu, Z. T. Wu, Y. Fan, and E. M. Tentzeris, "A miniaturized CSRR loaded wide-beamwidth circularly polarized implantable antenna for subcutaneous real-time glucose monitoring," *IEEE Antennas Wireless Propag. Lett.*, vol. 16, pp. 577–580, 2017.

Jungang Zhang (Student Member, IEEE) received the B.Eng. degree in automation from the Beijing Institute of Fashion Technology, Beijing, China, in 2019, with a focus on the design of wearable fabric electrodes and its front-end adjustment circuit for smart Electrocardiogram (ECG) sportswear, and the M.Sc. degree in electronics and electrical engineering from the University of Nottingham, Nottingham, U.K., in 2020. She is currently pursuing the Ph.D. degree with the Microelectronics Laboratory (meLAB), University of Glasgow, Glasgow, U.K.

She is involved in the project "CROSSBRAIN" funded by the European Innovation Council (European Commission) for developing tiny injectable robots capable of predicting and mitigating epileptic seizures. Her current research interests include wireless power transfer and data telemetry for self-reporting implantable medical devices.
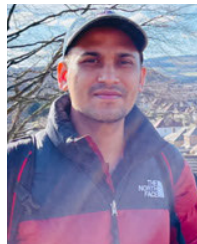
Rupam Das (Senior Member, IEEE) was a Marie Curie Fellow [EU H2020 MSCA-IF: Wireless, Scalable and Implantable Optogenetics for Neurological Disorders Cure (WiseCure)] with the Microelectronics Laboratory (meLAB), University of Glasgow, Glasgow, U.K. This fellowship focused on developing the wireless optogenetic systems based on metamaterials to treat brain diseases. He also worked as a Research Associate in a multimillion EU H2020 FET-Proactive "HERMES" project in Glasgow, where he was developing a flexible neural implant to treat epilepsy. Before moving to the U.K., he was a BK'21 Post-Doctoral Fellow with the University of Ulsan, Ulsan, South Korea, and the Applied Bioelectronics Laboratory (ABLab), Hanyang University, Seoul, South Korea. He is currently a Lecturer at the Department of Electronic Engineering, University of Exeter, Exeter, U.K. He is part of the Nano Engineering Science and Technology (NEST) and the Center for Metamaterial Research and Innovation (CMRI), Streatham Campus, University of Exeter, Exeter, U.K.

Dr. Das was also the Local Organizer of International Conference on Electronics, Circuits and Systems (ICECS) 2020 and a Session Chair Committee Member of ICECS 2022. He has served as a Guest Editor for *Philosophical Transactions of the Royal Society A*.

Daniel Hoare (Member, IEEE) received the bachelor's degree from the University of Wolverhampton, Wolverhampton, England, in 2017, the master's degree in cardiovascular disease from the University of Chester, Chester, England, in 2018, and the Ph.D. degree from the VascuSens Group, University of Glasgow, Glasgow, U.K., in 2022.

His Ph.D. degree was funded by the Engineering and Physical Sciences Research Council (EPSRC). His undergraduate degree was clinically based, where he was trained as a cardiac physiologist. He is currently a Post-Doctoral Researcher with the VascuSens Group, University of Glasgow. His field of interest is the integration of novel sensors into implantable medical devices and the validation of these proof-of-concept devices.

Huxi Wang (Student Member, IEEE) received the double B.Eng. degree in electrical and electronics engineering from the University of Electronic Science and Technology of China, Chengdu, China, and the University of Glasgow, Glasgow, U.K., in July 2020. He is currently pursuing the Ph.D. degree with the Microelectronics Laboratory (meLAB), James Watt School of Engineering, University of Glasgow.

Beyond his work in the meLAB, he was also a Fellow of the CRC 1261 project at Christian-Albrechts-Universität zu Kiel (CAU), Kiel, Germany, in 2022, where he worked on the development of magnetic modulated surface acoustic wave (SAW) sensors. His current research focuses on the development of ultra-low-noise readout circuits for spintronic sensors, with a particular emphasis on biomedical applications.

Afesomeh Ofiare received the M.Sc. and Ph.D. degrees in electronic and electrical engineering from the University of Glasgow, Glasgow, U.K., in 2009 and 2016, respectively.

He is currently a Post-Doctoral Researcher with the Ultrafast Group, Electronic and Nanoscale Engineering Division, University of Glasgow. His current research interests include high-frequency device characterization, antennas for millimeter-wave and THz applications, and wireless communications.

Nosrat Mirzai (Member, IEEE) managed a team of specialists for eight years and supervised for 18 years. From 1997 to 2007, he was the Deputy Manager of the Bioelectronics Unit, Institute of Biomedical and Life Sciences, focusing on the design development of advanced bespoke electronics for medical/biomedical and life sciences research applications. From 2007 to 2020, he was the Head of the Bioelectronics Unit, College of Medical, Veterinary and Life Sciences, University of Glasgow, Glasgow, U.K. He is the Former Head of the Bioelectronics Unit and is with the College of Medical, Veterinary and Life Sciences, University of Glasgow.

John Mercer received the B.Sc. degree (Hons.) in cell and molecular biology from Oxford Brookes University, Oxford, U.K., in 1995, and the M.Phil./Ph.D. degree in investigating the emerging role of p53 in radiation-induced mutations in thyroid cancer from the Berkeley, University of St Andrews, North Haugh, St Andrews, U.K., in 2000.

For his post-doctoral research, he joined the Addenbrooke's Hospital, Department of Medicine, University of Cambridge, Cambridge, U.K. He is currently a Senior Lecturer with the Institute of Cardiovascular and Medicine Science, University of Glasgow, Glasgow, U.K. He investigated the inducible role of p53 in vascular smooth muscle cell biology, with a significant emphasis on developing transgenic mouse models of diseases.

Hadi Heidari (Senior Member, IEEE) is currently a Professor of nanoelectronics with the James Watt School of Engineering, University of Glasgow, Glasgow, U.K, where his Microelectronics Laboratory (meLAB) conducts pioneering research on integrated microelectronics/nanoelectronics design for medical (wearables and implantables) and industrial (quantum computing and ultrasound systems) applications. His research has been funded circa £4M by major research councils and funding organizations, including the U.K. Research and Innovation (UKRI) (the Engineering and Physical Sciences Research Council (EPSRC) and Innovate UK), the European Commission, the Royal Society, British Council, the Scottish Funding Council, and the Royal Society of Edinburgh.

Dr. Heidari is a member of the RSE Young Academy of Scotland (YAS) and the eFutures Steering Group (an EPSRC-funded network representing the U.K.'s Electronic Systems Academic Community). He is a member of the EPSRC College and reviews proposals for the Croatian Science Foundation (HRZZ), the Swiss National Science Foundation (SNSF), and the Royal Society of New Zealand. He is a fellow of the Higher Education Academy (FHEA) and the Royal Society of Arts, Manufactures and Commerce (FRSA). He was a recipient of a number of awards, including the 2020 IET Healthcare Technologies Early Career JA Lodge Award, the 2019 IEEE Sensors Council Young Professional Award, the Rewards for Excellence Prize from the University of Glasgow in 2018, the Silk Road Award from the Solid-State Circuits Conference (ISSCC'16), the Best Paper Award from the IEEE International Symposium on Circuits and Systems (ISCAS'14) Conference, and the Gold Leaf Award from the IEEE International Conference on Ph.D. Research in Microelectronics and Electronics (PRIME'14) Conference.